Preprint typeset using LaTeX style emulateapj v. 5/2/11

arXiv:1411.7054v1 [astro-ph.SR] 25 Nov 2014

DISCOVERY OF LUMINOUS STAR FORMATION IN PMN 1452–5910/IRAS 14482–5857: THE PTERODACTYL NEBULA

Jones, D. I.[1] & Braiding, C. R.[2]

[1] Department of Astrophysics/IMAPP, Radboud University, Heijendaalseweg 135, 6525 AJ Nijmegen, The Netherlands. and
[2] School of Physics, University of New South Wales, 2052, Sydney, Australia.

ABSTRACT

We present sensitive 1–3 GHz ATCA radio continuum observations of the hitherto unresolved star forming region known as either IRAS 14482–5857 or PMN 1452–5910. At radio continuum frequencies, this source is characterised by a "filled-bubble" structure reminiscent of a classical HII region, dominated by three point sources, and surrounded by low-surface-brightness emission out to the $\sim 3' \times 4'$ source extent observed at other frequencies in the literature. The infrared emission corresponds well to the radio emission, with polycyclic aromatic hydrocarbon emission surrounding regions of hot dust towards the radio bubbles. A bright 4.5 μm point source is seen towards the centre of the radio source, suggesting a young stellar object. There is also a linear, outflow-like structure radiating brightly at 8 and 24 μm towards the brightest peak of the radio continuum. In order to estimate the distance to this source, we have used Mopra Southern Galactic Plane CO Survey ^{12}CO (1–0) and ^{13}CO(1–0) molecular line emission data. Integrated-intensity, velocity at peak intensity and line-fitting of the spectra all point towards the peak centred at $V_{LSR} = -1.1$ km/s being connected to this cloud. This infers a distance to this cloud of ~ 12.7 kpc. Assuming this distance, we estimate a column density and mass towards IRAS 14482–5857 of $\sim 1.5 \times 10^{21}$ cm^{-2} and 2×10^4 M$_\odot$, implying that this source is a site of massive star formation. Reinforcing this conclusion, our broadband spectral fitting infers dust temperatures of 19 and 110 K, emission measures for the sub-pc radio point-source of EM$\sim 10^{6-7}$ pc cm^{-6}, electron densities of $n_e \sim 10^3$ cm^{-3} and photon ionisation rates of $N_{Ly} \sim 10^{46-48}$ s^{-1}. The evidence strongly suggests that IRAS 14482–5857 is a distant – hence intense – site of massive star-formation.

Subject headings: ISM: clouds – HII regions – ISM: individual: (IRAS 14482-5857, PMN 1452-5910) – stars: early-type – stars: formation.

1. INTRODUCTION

Massive stars are the principle source of heavy elements in the universe, and disperse material and modify their environment through winds, massive outflows, expanding HII regions and supernovae (Zinnecker & Yorke 2007). This creates an important source of mixing and turbulence for the interstellar medium (ISM) of galaxies (Zinnecker & Yorke 2007), making massive star formation, and a theory for it, hugely important for modern astrophysics. For all their effect on their host galaxies, we understand little of the conditions of massive star formation, especially in the earliest phases. This is because, whilst a fully developed massive star or star cluster can be observed in the optical, as well as at other wavelengths, a high amount of dust extinction during their formation makes this a demanding proposition. Coupled with the fact that they are rare and possess short formation timescales, this makes observing the earliest phases of massive star formation in large numbers fiendishly difficult (Zinnecker & Yorke 2007).

Sites of massive star formation have traditionally been discovered using large surveys in the infrared, such as by using infrared colours (Molinari et al. 1996; Walsh et al. 1997), dust emission (Hill et al. 2005), or molecular line emission (Walsh et al. 2011; Burton et al. 2013). However, extending the distance to which sites of massive star formation in the Galaxy can be observed is necessarily difficult, due to the large regions that must be observed to a higher sensitivity. This is summarised by the statistic given by large surveys of mass as a function of distance that can be observed. For instance, the H_2O Galactic plane survey (HOPS) can detect a 20 K, 400 M$_\odot$ cloud at the 5σ level at 3.2 kpc, and a 3×10^4 M$_\odot$ clouds anywhere in the Galaxy (Walsh et al. 2011). Given this, it is becoming an imperative to use the ever-growing number of high-quality surveys across many wavebands to characterise star-forming region in a more systematic and comprehensive manner so as to increase the number of known massive star forming regions.

Here we report serendipitous radio continuum observations at 1–3 GHz, as well as an examination of the archival data towards what may be a hitherto unknown site of massive star formation; IRAS 14482–5857. A search of SIMBAD[1] within a radius of 2 arcminutes revealed only survey information for the radio (catalogued as PMN 1452–5910) and infrared source (catalogued) as IRAS 14482–5857, but nothing else[2]. The PMN 1452–5910 and IRAS 14482–5857 sources are positionally coincident, and hereafter we refer to this source simply as IRAS 14482–5857. Figure 1 shows IRAS 14482–5857, and its surrounding environment at 843 MHz from the Molongolo Observatory Synthesis (MOST; Bock et al. 1999) Galactic Plane Survey (MGPS; Mauch et al. 2003). IRAS 14482–5857 lies near the large ($40' \times 35'$) supernova remnant, G318.2+0.1, along the Galactic plane at a posi-

d.jones@astro.ru.nl

[1] http://simbad.u-strasbg.fr/simbad/

[2] SIMBAD cites an X-ray study (Bocchino et al. 2001) in reference to PMN 1452–5910, but which only contains the source IRAS 14498–5856. This reference is spurious.

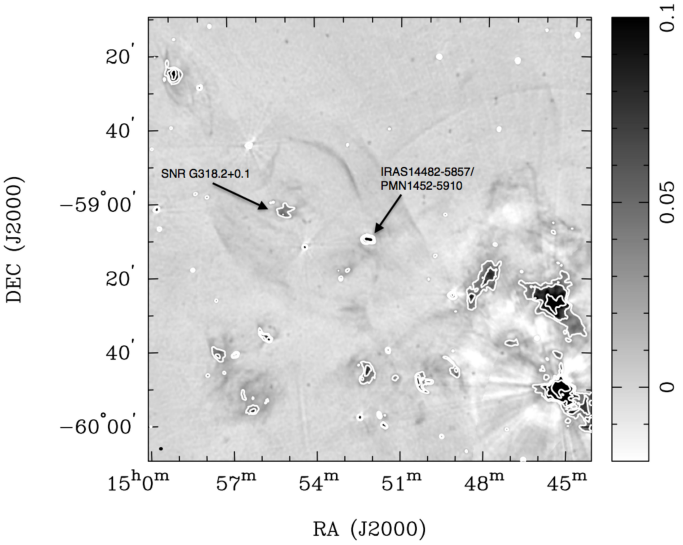

FIG. 1.— 843 MHz total intensity image of the region surrounding IRAS 14482–5857, overlaid with the same (white) contours at 30 (=5σ), 60, 120, 240, and 480 mJy/beam. The beam at this declination is $43'' \times 50''$, and is shown in the lower-lefthand corner.

tion of $\alpha = 14^{\rm h}52^{\rm m}05\overset{\rm s}{.}3$, $\delta = -59°10'08\overset{''}{.}58$ (J2000.0).

2. NEW OBSERVATIONS AND ARCHIVAL DATA

In this section we describe the new data on IRAS 14482–5857 that was obtained using the ATCA, as well as the archival data obtained during a literature search, as well as survey data that we possessed.

2.1. *New Australia Telescope Compact Array Data*

The ATCA data presented here are a part of an observational campaign towards a nearby object, but IRAS 14482–5857 is contained within the field of view at 1–3 GHz. The observations and data reduction technique will be detailed elsewhere, but we give a brief overview here.

A (hexagonal) mosaic observation of the region were performed with the ATCA on the 5$^{\rm th}$ May and 6$^{\rm th}$ September 2013 in the 6.0C and 1.5A array configurations, respectively. Both array configurations have a minimum baseline of 153 meters, up to a maximum of 6000 meters (6.0C configuration only – the maximum 1.5A baseline is 4469 meters). The observations used the 16cm receiver with the CFB 1M-0.5k correlator, which gives a 2 GHz bandwidth with 2048 channels of 1 MHz width over the 1–3 GHz band. We split up the band into four 512 MHz-wide sub-bands, and use only the 1332, 1844 and 2868 MHz bands here. Standard calibration and imaging methods were used within the MIRIAD software reduction package. The flux density calibrator used was PKS B1934–638, bootstrapped to a flux density of 11.986 ± 0.005 Jy/beam at 2100 MHz. These bands have a resolution of $10.6'' \times 6.8''$, $\sim 8.6'' \times 5.4''$ and $5.1'' \times 3.4''$ and 1σ r.m.s. sensitivities of $\sim$ 400, $\sim$ 200 and $\sim$ 100 μJy/beam at 1332, 1844 and 2868 MHz, respectively. We found a systematic uncertainty of $\sim$ 5% for the observations and all errors quoted in this paper use this added in quadrature to the local r.m.s. sensitivity. It is important to note that these observations will recover spatial information only up to $\sim 5.5'$, $\sim 4'$ and $\sim 2.7'$ at 1332, 1844 and 2868 MHz. Given that the source size is $\sim 3' \times 4'$, the upper band may not fully recover the entire flux density.

2.2. *Archival Data*

In order to better characterise the IRAS 14482–5857 source, we have performed a literature search, as well as obtained data from several surveys. Here we describe the data products we have obtained and used.

2.2.1. *Millimeter & Infrared Data*

Since this source is identified in SIMBAD as IRAS 14482–5857, we know that it is detected at infrared frequencies. Hence we have obtained mid-infrared data from Infrared Astronomical Satellite (IRAS) at 12, 25, 60 and 100 μm. We have also obtained IRAC Mid-course Space eXperiment (MSX) and *Spitzer* Galactic Legacy Infrared Mid-Plane Survey Extraordinaire (GLIMPSE) data at the shorter wavelengths of 8.28, 12.13, 14.65, and 21.34 μm for the A, C, D and E bands of MSX and at 3.6, 4.5, 5.8 and 8 μm for the GLIMPSE bands. Emission at 3.6 μm is dominated by stellar emission, and is usually represented in 3-colour (i.e., false-colour) images as blue. Bright emission at 4.5 μm is thought to be due to shocks arising from outflows from protostellar objects interacting with the ambient ISM (Cyganowski et al. 2008). 5.8 and 8.0 μm emission is thought to be due to polycyclic aromatic hydrocarbons (PAHs), which are particularly useful for highlighting dust emission, since they are very sensitive to infrared emission (Churchwell et al. 2009). We have also made use of the longer wavelength MIPSGAL 24 μm emission, which also traces dust emission. Finally, we have searched archival papers for information on dust clumps observed at 1.1 mm (150 GHz), which is also thought to be a powerful discriminator of the evolutionary stage of massive star formation (see, for instance, Breen et al. 2010b).

2.2.2. *Mopra ^{12}CO(1–0) and ^{13}CO(1–0) data*

In order to establish the presence (or absence) of molecular gas towards IRAS 14482–5857, we have obtained molecular line emission data from the Mopra telescope from the Mopra Southern Galactic Plane CO Survey (Burton et al. 2013). This survey used the Mopra telescope, which is a single 22 m dish radio telescope located $\sim$ 450 km north-west of Sydney, Australia (31°16′04″S, 149°05′59″E, 866-m a.s.l.) to survey a region of the southern Galactic plane from $l = 305° - 345°$ and $b = \pm 0.5°$. The survey observations utilised the UNSW Mopra wideband spectrometer (MOPS) in zoom mode with the 3 mm receiver, which operates in a frequency range of 77–117 GHz, and for the relevant observations here, the 8 GHz-wide bandwidth was centred on 112.5 GHz. The fast-mapping zoom mode of MOPS allows observations in up to 8 windows simultaneously, where each window is 137.5 MHz wide and contains 4096 channels in each of two polarisations. This observational set-up yields a spectral resolution of $\sim$ 0.09 km/s over a velocity range of ~ -500 to 500 km/s depending on the line sampled, and a spatial resolution of $\sim 35''$, with the main beam efficiency of 0.55 at 115 GHz. The observations were conducted using the 'fast on-the-fly' (FOTF) method, and reduced as per the methods described in Burton et al. (2013). This resulted in a 1σ sensitivity for the ^{12}CO and

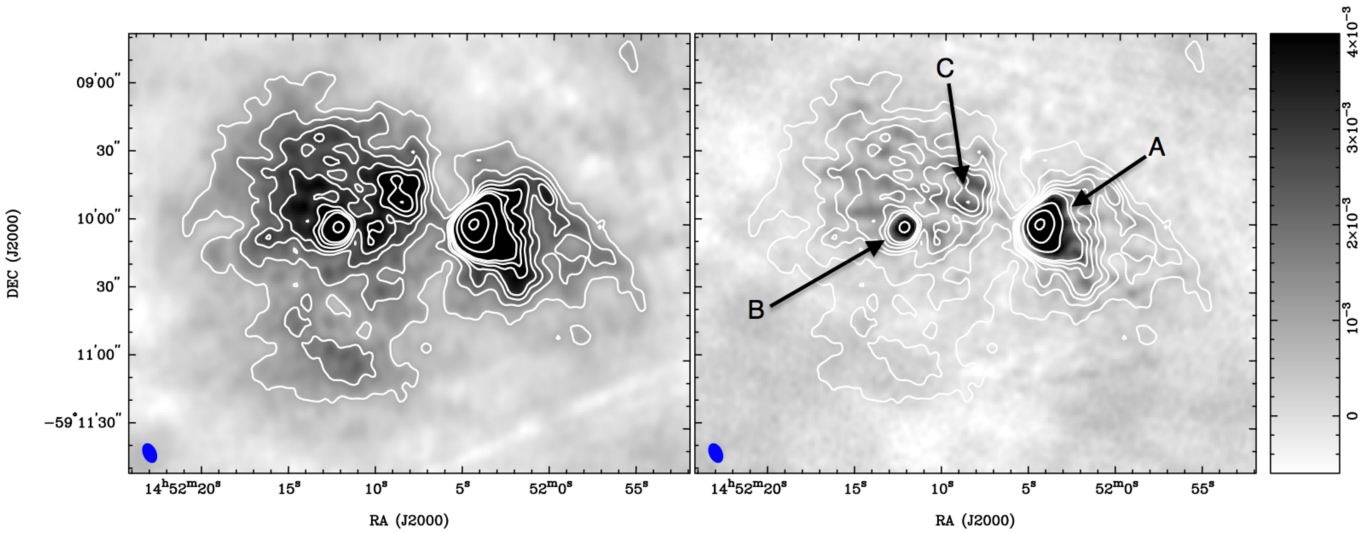

FIG. 2.— Total intensity images of our ATCA data at 1844 (left) and 2868 (right) of IRAS 14482–5857. The contours in both frames are 1844 MHz contours at 0.8, 1, 2, 4, 6, 7, 8, 10, 20, 40, and 80 mJy/beam. The intensity scale is linear and runs from -0.6 to 4 mJy/beam. At 1844 MHz, the r.m.s. noise is ~ 200 μJy/beam (so that 0.8 mJy/beam $= 4\sigma$), whereas at 2868 MHz, the r.m.s. noise is ~ 100 μJy/beam. The beams are $8.6'' \times 5.4''$ and a position angle of 25.1° and $5.1'' \times 3.4''$ at a position angle of 21.6° at 1844 and 2868 MHz respectively. The beam are shown in the lower-lefthand corner of both images. The regions that are peaks in intensity are labeled 'A', 'B', and 'C' in the righthand panel.

^{13}CO (hereafter simply 12CO and 13CO) lines of ~ 1.5 K and ~ 0.7 K per 0.1 km/s velocity channel, respectively.

2.2.3. *NH_3 (1,1) and (2,2) inversion transition and H_2O maser emission*

As presaged above, it is thought that massive stars are formed in dense clumps of cold gas. Since CO is known to not be a particularly good tracer of cold, dense molecular material because it "freezes out" in temperatures of 10s of K (Nicholas et al. 2011), as well as suffering optical depth problems at moderate densities, we have obtained data from the H_2O Galactic Plane Survey (HOPS; Walsh et al. 2011).

HOPS is a survey of $\sim 100°$ region of the Galactic plane (from $-70° > l > 30°$, $|b| < 0.5°$) using the Mopra telescope in the 12-mm waveband in on-the-fly mode also using MOPS. HOPS is particularly useful for tracing massive star formation because in a single survey, it traces the 23 GHz water maser transition that is known to trace star formation, as well as the versatile inversion transitions of the ammonia molecule (which do not suffer from freeze-out, and trace cold, dense clumps). The NH_3 (1,1) and (2,2) data have a resolution of 2′ over velocities ranging from ±200 km/s. The median sensitivity of the NH_3 data cubes is $\sigma_{T_{mb}} = 0.20 \pm 0.06$ K.

3. RESULTS

3.1. *Radio Continuum Emission*

Figure 2 shows total intensity radio continuum images of IRAS 14482–5857 at 1844 and 2868 MHz. The source exhibits a bi-lobal structure, consisting of diffuse, low-surface-brightness emission, as well as at least three strong peaks, with a single peak seen in the western lobe of the bubbles, and two in the eastern one. The lack of diffuse emission at 2868 MHz in Figure 2 (right), shows the results of the spatial filtering of interferometers. However, we suggest that the difference between the true flux density distribution of the source and that shown here is not significant. This is because, as is shown in Table 1, the integrated flux densities of the strong point sources are consistent with optically-thin thermal emission, and match those seen at lower (843 MHz) and higher (4500 MHz) frequencies. Spectral index maps (see below) also show optically-thin thermal emission over most of the bubbles, suggesting that significant amounts of flux at 2868 MHz have not been filtered. At 1332 MHz, as Figure 3 shows, the opposite is true. This figure shows IRAS 14482–5857 at 1332 MHz, and illustrates that there is ample diffuse emission at this frequency, since it samples structures larger than the source itself. Indeed, the larger source extent, along with an integrated flux density for the entire source of ~ 2 Jy suggests that at this frequency, a significant amount of background emission from the Galactic plane is being sampled. Hence we do not use this datum in fitting the centimetre radio continuum emission. Again – although in the opposite sense – the flux density reported from the PMN survey at 4500 MHz (using single dishes) is commensurate with the 1844 and 2868 MHz flux densities shown in Table 1. Hence we conclude that the additional flux density in the 1332 MHz is background emission, rather than reflecting additional flux density from the source itself.

Figure 4 shows a spectral index map of IRAS 14482–5857 between 1844 and 2868 MHz. We define the spectral index α between two frequencies ν as $\alpha \equiv d \log S_\nu / d \log \nu$. Figure 4 shows the spectral index variations between -1 (indicative of non-thermal emission, e.g., synchrotron emission) and $+2$ (indicative of thermal emission, e.g. optically thick thermal emission). This indeed illustrates the point made above, that IRAS 14482–5857 consists of optically thin thermal emission, interspersed with some non-thermal emission towards the edge of the radio bubbles, which is most likely due to low signal-to-noise in the 2868 MHz data. The same map between 1332 and 1844 MHz shows a similar spectro-morphological structure to that shown in Figure 4, but with steeper spectral indices, suggestive of contaminating flux density.

We have characterised the strong peaks observed at

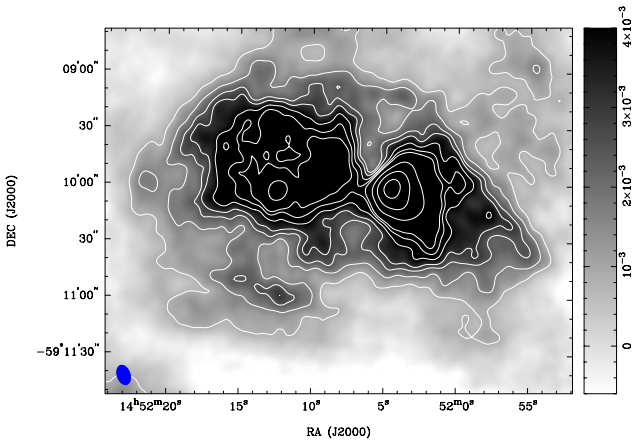

FIG. 3.— Total intensity image of IRAS 14482–5857 at 1332 MHz. The (white) contours are at levels of 0.2, 0.4, 0.8, 1, 2, 4, 8, 16, 32, and 64 mJy/beam. The intensity scale is linear and runs from -2 to 6 mJy/beam. The r.m.s. noise is ~ 400 μJy/beam (first contour is 0.8 mJy/beam $\sim 2\sigma$). The beam is $10.6'' \times 6.8''$ and a position angle of 18.8° and is shown in the lower-lefthand corner.

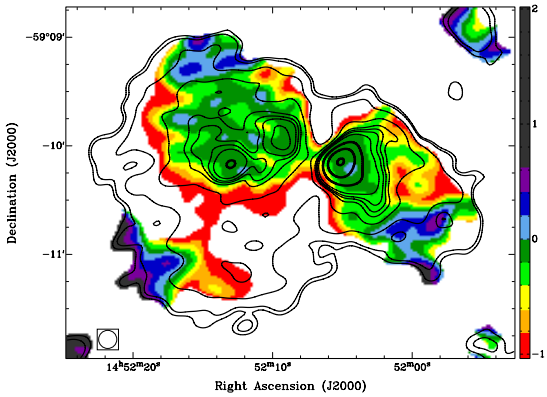

FIG. 4.— Spectral index map of IRAS 14482–5857 between 1844 and 2868 MHz at a common resolution of $10'' \times 10''$. The (black) contours are 1844 MHz emission at 0.8, 1, 2, 3, 4, 5, 6, 7, 8, 12 and 16 mJy/beam. This illustrates the non-thermal nature of parts of the radio bubbles. The peaks of intensity within the radio bubbles show a thermal structure, commensurate with the total integrated flux.

1332, 1844 and 2868 MHz, and labelled as sources A, B and C in the right-hand panel of Figure 2. This was done by fitting Gaussian sources to the data using the MIRIAD task *imsad*, without fitting a background to subtract. We do not subtract any background emission because, as shown above, the size scales that these observations trace are not larger than the source, and hence we would only be subtracting source flux density. A more careful analysis would take this into account at 1332 MHz, however. Table 1 shows the results of this fitting, and shows the source name (column 1), frequency fitted (column 2), best-fit positions (columns 3 and 4), angular sizes and position angles (column 5) of the best-fit Gaussians, as well as the peak and integrated flux density (columns 6 and 7). As can be seen in Figure 2 (right), the second peak in the eastern bubble is not detected at 2868 MHz. The diffuse flux density has average values of 6, 3 and 3 mJy/beam at 1332, 1844 and 2868 MHz respectively, with the stronger average flux density at 1332 MHz probably due to the background flux density at scales larger than the source. These levels were used as a cut-off level for the modelling of the bright radio peaks.

3.2. *Archival Data*

3.2.1. *Radio Continuum and Millimetre Data*

Data associated with PMN 1452–5910 comes from the Parkes-MIT-NRAO survey (PMN; Wright et al. 1994) and comprises a flux density and angular extent of 1.14 ± 0.06 Jy and $3' \times 4'$ at a position angle of 128.5°, respectively.

A SIMBAD search of IRAS 14482–5857 contains flux densities from a coincident source found using the QUaD telescope from their Galactic plane survey (Culverhouse et al. 2010), which lists a flux density of 2.35 ± 0.44 and 1.90 ± 0.3 Jy at 100 and 150 GHz, respectively (Culverhouse et al. 2011). This flux density comes from a source extent of $3.9' \times 3.1'$ and $2.8' \times 1.7'$ at 100 and 150 GHz respectively, roughly matching that found at centimetre wavelengths (i.e., the PMN survey and the extent of the source in Figure 1). Culverhouse et al. (2011) also characterise this source as an UCHII region based on the Wood-Churchwell criteria which is based on the IR colours (Wood & Churchwell 1989).

3.2.2. *Mopra CO(1–0) Molecular Line Emission*

Figure 5 shows an integrated-intensity (i.e., *mom*0) image for the 12CO data integrated over the velocity range of -10 to +10 km/s. This velocity-range is motivated by inspection of velocity-at-peak-intensity images (not shown here) derived for this region that show that the peak of emission within the (white) contours of Figure 5, as well as the more extended emission, lie between this velocity range. Integrating the 12CO emission between -55 and -35 km/s (images also not shown here) does not reveal emission that follows the same morphology as Figure 5. This suggests that the material located near 0 km/s is associated with IRAS 14482–5857. On the other hand, Figure 5 shows the positional coincidence of the peak of emission of both the 12CO and radio continuum (peaks A and B of Figure 2). This Figure also illustrates the extension of the molecular emission to the southeast of the radio source, and its termination in a linear-like feature running roughly northeast to southwest and represented by the tight grouping of the contours found there.

Figure 6 shows the line profile for the 12CO emission towards the peak of the radio emission at 1844 MHz, given as source A in Figure 2 (*right*). We have fit (using an iterative χ^2 fitting procedure) the resulting spectrum for this position and find that a two-plus-one component fit represents the data best. We fit a two-component Gaussian to the ~ -42 km/s line emission, one at $V_{LSR} = -41.6 \pm 0.2$ km/s with a brightness temperature of $T_{mb} = 4.0 \pm 0.1$ K and a full-width at half-maximum (FWHM) of $\sigma_{FWHM} = 2.1 \pm 0.1$ km/s. The second peak is fit using a brightness temperature of $T_{mb} \sim 3.1 \pm 0.2$ K at a velocity of $V_{LSR} = -50.2 \pm 0.2$ km/s at a FWHM of $\sigma_{FWHM} = 1.3 \pm 0.1$ km/s. The peak of emission at ~ 0 km/s is fit

TABLE 1
OBSERVED PARAMETERS OF THE SOURCES WITHIN IRAS 14482–5857 AT 1332, 1844 AND 2868 MHZ AS MARKED IN FIGURE 2.

Source	Frequency (MHz)	α (J2000.0)	δ (J2000.0)	Angular Size/P.A. ($''$,°)	I_ν (mJy/beam)	S_ν (mJy)
(1)	(2)	(3)	(4)	(5)	(6)	(7)
A	1332	14:52:04.26	-59:10:03.0	20.4 × 18.5, -5.1	51.9 ± 0.3	272 ± 13
	1844	14:52:04.34	-59:10:01.9	15.6 × 13.1, -15.8	45.2 ± 0.2	200 ± 10
	2868	14:52:04.35	-59:10:01.5	11.9 × 10.0, -16.0	23.0 ± 1.0	155 ± 8
B	1332	14:52:11.06	-59:09:56.8	106.1 × 48.9, -71.1	8.4 ± 0.4	606 ± 30
	1844	14:52:11.51	-59:09:56.8	90.6 × 44.1, -69.8	4.8 ± 0.2	418 ± 21
	2868	14:52:12.25	-59:10:02.8	07.9 × 07.3, -46.7	7.7 ± 0.4	25 ± 1
C	1332	14:52:13.20	-59:09:46.4	43.1 × 22.6, 1.9	6.1 ± 0.3	82 ± 4
	1844	14:52:00.37	-59:09:47.7	20.1 × 10.0, +29.0	3.6 ± 0.2	16 ± 1

NOTE. — Units of right ascension are hours, minutes and seconds, and units of declination are degrees, minutes and seconds.

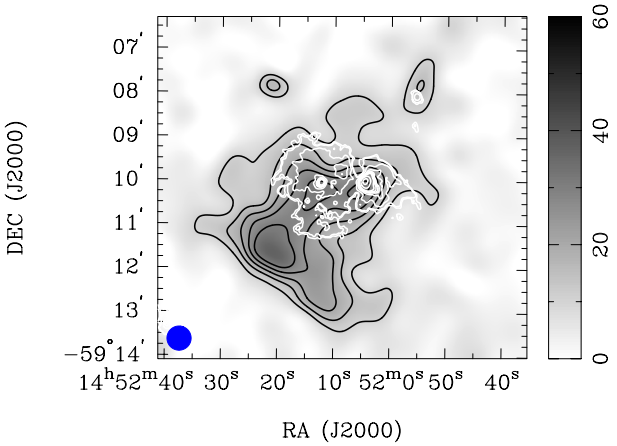

FIG. 5.— Integrated-intensity image of the region surrounding IRAS 14482–5857 obtained using the velocity-cube for the 12CO-line and integrated over the velocity range of -10 to +10 km/s, overlaid with the same contours at 10, 15, 20, 25, 30 and 35 K km/s (the peak emission is at 35 K km/s). Overlaid on the integrated-intensity image are (white) contours of our 1844 MHz ATCA data, using the same contours as in Figure 2. The intensity range (for a linear scaling) runs from 0 to 60 K km/s, so as to illustrate the peaks of emission coinciding with the radio continuum peaks. The 35″ beam of the 12CO emission is shown in lower left-hand corner.

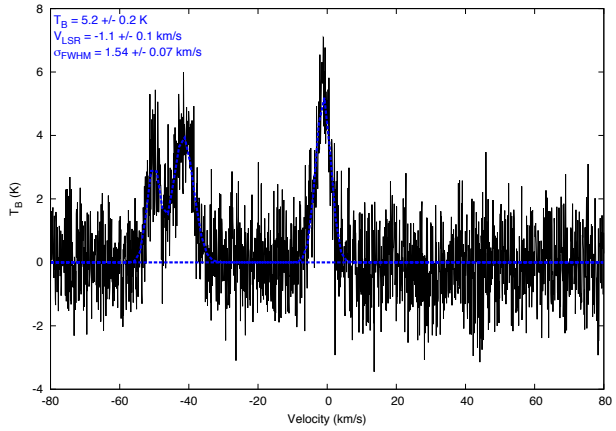

FIG. 6.— Brightness temperature versus velocity plot for the 12CO emission towards the peak of the emission found towards IRAS 14482–5857, as shown in Figure 5. The derived parameters for the fit to the data (as shown by the – blue – dashed line) for peaked emission at -1.12 ± 0.1 km/s are shown in the top left-hand corner of the plot.

using a brightness temperature of $T_{mb} = 5.2 \pm 0.2$ K, at a velocity of $V_{LSR} = -1.1 \pm 0.1$ km/s and a FWHM width of $\sigma_{FWHM} = 1.5 \pm 0.1$ km/s. This fitting shows that, in addition to the peak-velocity analysis described above, the emission component at $V_{LSR} = -1.1 \pm 0.1$ km/s is stronger than the $V_{LSR} = -41.6, -50.2$ km/s components. Using the 13CO data cube, we have similarly fit the emission from the peak of the radio continuum. Although the weaker nature of the lines here means that we could not reliably fit any emission around the −42 km/s line seen in the 12CO cube, we could fit a component to the emission around −1.1 km/s. Doing this results in parameters of $T_{mb} \sim 1.4 \pm 0.1$ K at a velocity centroid of $V_{LSR} = -0.9 \pm 0.1$ km/s and a FWHM width of $\sigma_{FWHM} = 1.0 \pm 0.1$ km/s. Using the velocity at peak intensity for each of the components in the 12CO data, and assuming that IRAS 14482–5857 is indeed associated with these clouds, we derive near (far) distance estimates of ∼ 3.5(9.0) kpc and 2.85(9.75) kpc for the −50.2 and −41.6 km/s peaks respectively and ∼ 12.7 kpc for the −1.1 km/s peak.

3.2.3. *H_2O Maser and Ammonia Line Emission*

From the HOPS data and catalogue (Walsh et al. 2011), we find that a water maser source with a peak flux density of 5.1 Jy at -3.3 km/s with a line-width of 1.0 km/s is catalogued at a position of (R.A., Dec.; J2000.0)=$14^h52^m14.5^s, -59°10^m49.0^s$. From the given conversion factor of 12.5 at 22.2 GHz, this flux corresponds to a main beam brightness temperature of 0.4 K.

Figure 7 shows the velocity-integrated emission (integrated between -10 and +10 km/s) towards IRAS 14482–5857. In addition to the position of the maser emission reported in Walsh et al. (2011), which is described by the (red) cross, it shows two regions of possible maser emission. The first peak (at ∼ 2.7 K km/s) is located at $\alpha = 14^h52^m17^s.8$, $\delta = -59°10'50''.2$ (J2000.0), and is the maser emission reported above. The second peak (at ∼ 2.3 K km/s) is located at $\alpha = 14^h51^m58^s.3$, $\delta = -59°09'50''.2$ (J2000.0), which is located ∼ 2.7′ angular distance from the reported maser spot, which is a separation of about 1.2 beams. Thus, we take only the listed brightness temperature, velocity and velocity width

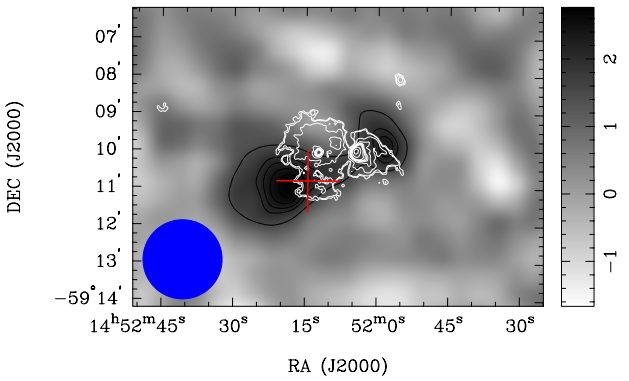

FIG. 7.— Velocity-integrated image of 22.2 GHz H_2O maser emission surrounding IRAS 14482–5857. The emission seen here has been integrated between -10 and +10 km/s, and is overlaid with the same (black) contours at 1.5, 2, 2.2, 2.4, and 2.6 K. The (red) cross represents the maser emission reported by the HOPS collaboration (Walsh et al. 2011). The (white) contours are 1844 MHz radio continuum emission at 0.8, 1, 2, 4, 8 and 16 mJy/beam. The 2′ Mopra beam for the HOPS data is shown in the lower left-hand corner.

listed in Walsh et al. (2011), suggesting that observations with a higher angular resolution instrument such as the ATCA is required to reveal the nature of the H_2O maser emission throughout IRAS 14482–5857.

Using a velocity centroid of $v = -3.3$ km/s, and assuming that this source is associated with the radio emission, we arrive at a distance to IRAS 14482–5857 of 12.5 kpc. This is similar to the distance derived above from the 12CO emission, and hereafter, we adopt a distance to IRAS 14482–5857 of 12.5 kpc. This implies that the source extent results in an intrinsic source size of $\sim 11 \times 14.5$ pc.

Utilising the publicly available data cubes from the HOPS website[3], we have searched for emission from the inversion transitions of the NH_3 (1,1), (2,2) and (3,3) lines. We found no emission coincident with the IRAS 14482–5857 source at either velocity down to the limiting $\sigma_{T_{mb}} = 0.20 \pm 0.06$ K. For the near distance, HOPS would observe a 400 $M_\odot$ cloud here with a 5σ level (whereas this increases to $\sim 10^4$ $M_\odot$ at the far distance). Interestingly, for the (1,1) transition, this equates to a 3.2 kpc distance limit for detecting a 20 K, 400 $M_\odot$ cloud at the 5σ level, with more massive clouds being observable further away with a 3×10^4 $M_\odot$ cloud being observed anywhere in the Galaxy. We note that even though H_2O maser emission has been known to appear at velocities far from the systemic velocity of the source that created it (Breen et al. 2010a), the strong 12CO lines fitted in the previous section suggest that this is not the case here.

3.2.4. *Other Masing Emission Surveys*

Maser searches, particularly the 6.7 GHz methanol maser line first detected by Menten (1991) over 20 years ago, are excellent discriminators of massive star forming regions. Indeed, it has recently been shown that this masing transition is exclusively associated with massive star formation (Breen et al. 2013). However, surveys searching for 6.7 GHz methanol masers have not detected any significant maser emission from the region down to a limiting flux density of 0.3 Jy, for a beam size of 3.3′ (Walsh et al. 1997). We have searched the literature for other observations of this region using other maser tracers, class I methanol masers at 33 and 44 GHz (Voronkov et al. 2014). No survey, other than HOPS, has reported maser emission from IRAS 14482–5857 (i.e., the methanol maser surveys – e.g. Caswell 1998; Green et al. 2012).

3.3. *Infrared Emission*

Figure 8 presents a 3-colour image of IRAS 14482–5857 at 3.6 (blue; GLIMPSE/IRAC), 8 (green; GLIMPSE/IRAC) and 24 μm (red; MSX/MIPS).

This image shows a complex source morphology. The medium surrounding IRAS 14482–5857 is dominated by 8 μm emission, which is sensitive to polycyclic aromatic hydrocarbon (PAH) emission, and a strong tracer of massive star formation (Tielens 2008). This PAH emission is wispy and filamentary in nature, extending some $\sim 1-2'$ further than, and appears to confine, the radio emission. The extension of the diffuse radio continuum emission towards the southwest and southeast of the source follows minima of the PAH emission. Hot dust emission, traced by the 24 μm emission, is most obviously seen within the diffuse radio filled bubble morphology of a classical HII region of this source, although this is mixed with significant amounts of PAH emission, giving large parts of the bubbles the yellow colour seen in the image. The southwest bubble extends further out, and matches low-surface brightness emission traced by hot dust emission.

Figure 9 shows a closeup of the radio bubble-structures of IRAS 14482–5857. The levels in this figure have been adjusted to bring out the detail in the emission in the bubble, which was saturated in Figure 8, so as to illustrate the low-surface-brightness and filamentary nature of the PAH emission surrounding the object. Figure 9 shows that the southeast bubble is dominated by dim emission from hot dust, which is surrounded by PAH emission, particularly towards the centre of the source, where the filled bubbles are observed to pinch together in the radio continuum. This behaviour is also seen in the western bubble, although it is smaller and the dust emission is brighter and dominated by a strong point source at 24 μm. The central regions of IRAS 14482–5857 again show dust/PAH dominated emission, which is aligned in a direction perpendicular to the extension of the diffuse radio bubble.

Figure 10 shows a closeup of the central regions of IRAS 14482–5857. It reveals that at the point where the radio bubbles pinch and meet is a blue, compact source dominated by 3.6 μm emission, suggesting that this is a young stellar object (YSO). This object appears to be surrounded by a cocoon of hot dust emission with at least one linear feature, reminiscent of an outflow that is yellow in colour, suggesting that it results primarily from PAH and hot dust emission. It is interesting, and maybe significant, that this outflow-like structure is pointing towards the strongest peak of radio emission in the western bubble. A commensurate feature is not observed, however, towards the eastern bubble, which exhibits very low-surface-brightness PAH emission, again in the direc-

[3] This can be found at: http://awalsh.ivec.org/hops/public/index.php

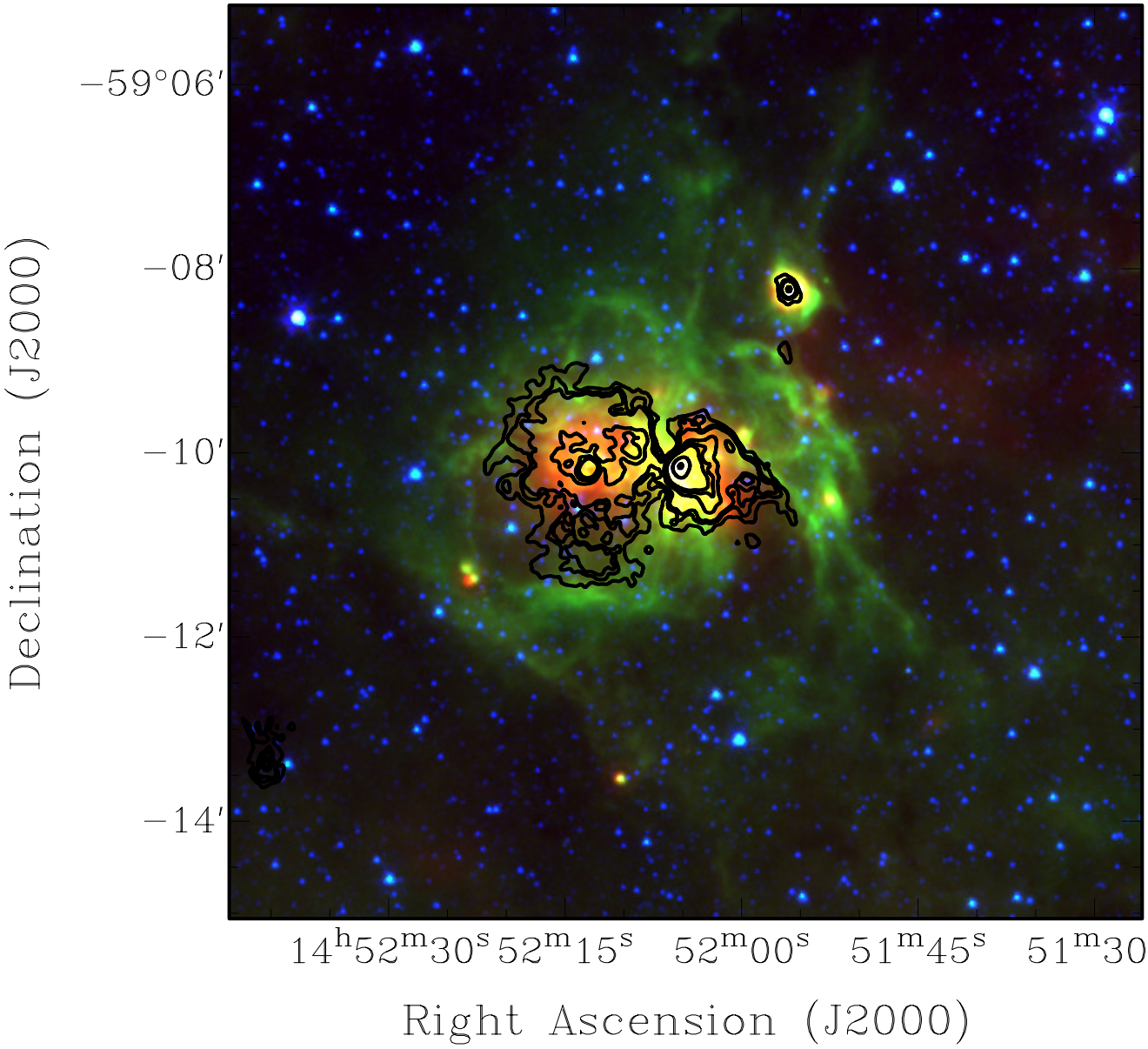

FIG. 8.— A 3-colour image of the region surrounding IRAS 14482–5857 obtained using 3.6 μm (blue), 8 μm (green) data from the GLIMPSE survey, as well as 24 μm (red) data from MIPS. The 24 μm emission runs from 6 to 162 MJy/sr, whilst the 3.6 and 8 μm emission runs from 0.3 to 24.5 and 27 to 127 MJy/sr, respectively under a linear transfer function. The contours, now black and at levels starting at 0.8 mJy/beam increase as $0.8 * 2^n$ for $n \in [1, 8]$, in order to maximise clarity in the 3-colour image.

tion perpendicular to the bubble-structures observed in our radio continuum data.

Figure 11 shows the region at 4.5 μm, thought to be due to shocked molecular hydrogen and CO band heads, which possibly indicates the presence of an outflow (Hindson et al. 2012). It is instructive, then, that the 4.5 μm emission from this region is bright, and concentrated near the central compact object (seen as the bright blue emission in Figure 10) and the brightest of the radio continuum emission regions. This perhaps demonstrates that this object possesses an outflow (Cyganowski et al. 2008).

Table 2 summarises the flux densities in the FIR waveband derived by the integration within the lowest contour of the radio emission at 1844 MHz. We find flux densities of 15, 10, 27 and 43 Jy at the A, C, E and D bands of MSX.

4. DISCUSSION

4.1. *Spectral Energy Distribution*

Figure 12 shows the spectral energy distribution of IRAS 14482–5857 from 843 MHz up to 3.6 μm. The SED shows that the emission at FIR frequencies long-ward of ~ 8 μm is due to thermal dust emission, whilst the radio continuum emission is well fitted with an optically thin thermal bremsstrahlung model. The FIR and dust emission were fitted with a two-component "greybody" model, which is a modified blackbody curve, where the opacity is assumed to vary with frequency as $\tau_\nu = (\nu/\nu_0)^\beta$, where ν_0 is the frequency at which the optical depth of that component is unity. The flux density is then modelled according to $S_\nu = B_\nu(T_d)[1-\exp(-\tau_\nu)]\Omega_S$, where $B_\nu(T_d)$

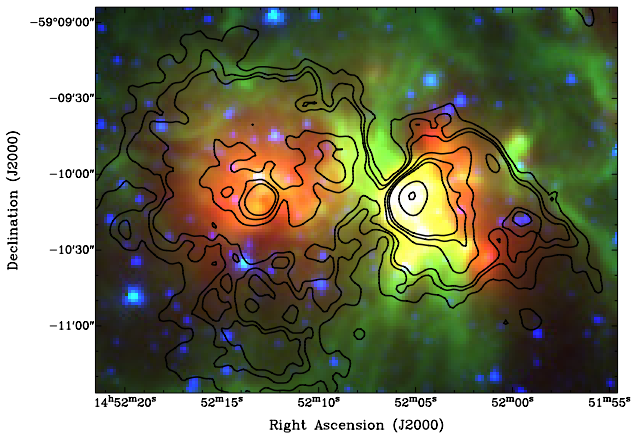

FIG. 9.— Closeup of the diffuse radio emission of IRAS 14482–5857. The colours are the same as in Figure 8, with the red and green levels adjusted to bring out specific features observed within the bubble. Specifically the 24 μm levels are now from 6 to 237.5 MJy/sr, whilst the 8 μm emission is from 28 to 154 MJy/sr. The radio contours are the same 1844 MHz ATCA contours as in Figure 8.

TABLE 2
OBSERVED PARAMETERS OF THE SOURCES WITHIN IRAS 14482–5857 IN THE FIR.

Frequency (μm) (1)	Average Flux Density (Jy/sr) (2)	Integrated Flux Density (Jy) (3)
3.6[a]	6.3	38
4.5[a]	4.9	29
5.8[a]	26.4	158
8.0[a]	73.7	443
8.28[b]	14.8	15
12.0[c]	30.7	31
12.13[b]	9.9	10
14.65[b]	26.7	27
21.34[b]	42.7	43
25[c]	53.7	54
60[c]	192	470
100[c]	1302	1315

[a] IRAC/GLIMPSE data
[b] MSX
[c] IRAS

is the Planck function at the dust temperature, T_d, and Ω_S is the solid angle subtended by the dust emitting part of the source (i.e., the region interior to the PAH emission in Figure 8 and commensurate with the lowest radio continuum contour). In the fitting, we have used an opacity index, β of 2.0, following Garay et al. (2002) for sources with limited spectral points and consistent for sources showing signs of high-mass star formation (Ossenkopf & Henning 1994). We find a cold dust component at 19 K for an angular size of $3' \times 4'$, assuming a Gaussian flux distribution within the source, and an optical depth of unity at 27 μm. The hot dust component is well-fitted with a temperature of 110 K.

The radio continuum emission below $\sim$ 100 GHz is well fit with an optically thin free-free emission, and to fit the emission, we used a technique of "bootstrapping" the thermal flux density (Crocker et al. (2010), Supplementary information) to that given by the 4500 MHz PMN 1452–5910 datum, F(4500 MHz), and assuming that it is completely thermal, so that the optical depth at 4500 MHz, τ(4500 MHz) is given by:

$$\tau(4500\ \mathrm{MHz}) = \frac{F(4500\ \mathrm{MHz})}{\Omega_S B(4500\ \mathrm{MHz}, T)}, \qquad (1)$$

where Ω_S is the solid angle of the source, and $B(4500\ \mathrm{MHz}, T)$ is the Planck function at temperature, T. We then obtain the optical depth at frequency ν from:

$$\tau_\nu = \tau(4500\ \mathrm{MHz}) \left(\frac{\nu}{10\ \mathrm{GHz}}\right)^{-2.1}. \qquad (2)$$

Hence the flux density, S_ν at any frequency is:

$$S_\nu = \Omega_S B(4500\ \mathrm{MHz}, T)[1 - e^{-\tau_\nu}]. \qquad (3)$$

Using a nominal electron temperature of 10,000 K, we fit the thermal emission. The total luminosity radiated by from the source as a whole, found from integrating the emission shown in Figure 12 from 10 MHz up to 1 THz is $\sim 3 \times 10^5$ L$_\odot$.

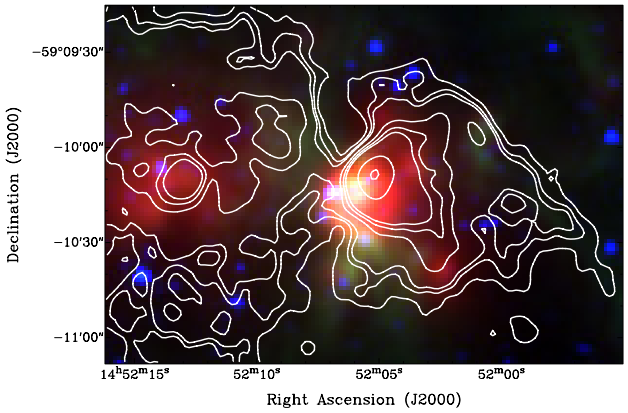

FIG. 10.— Closeup of the central region of IRAS 14482–5857. The colours are the same as in Figure 8, with the levels adjusted to bring out specific features observed within central parts of the source. Specifically the 24 μm levels are now from 30 to 540 MJy/sr, whilst the 8 and 3.6 μm emission runs from 25 to 550 MJy/sr and 20 to 40 MJy/sr, respectively. The (white) radio contours are the same 1844 MHz ATCA contours as in Figure 8.

4.2. *Derived Parameters*

4.2.1. *Mass Estimate from Dust Emission*

Following Garay et al. (2002), the fact that the thermal dust emission at 150 GHz is optically thin implies that the mass of the cloud, M_g can be estimated:

$$M_g = \frac{S_\nu D^2}{R_{dg} \kappa_\nu B_\nu(T_d)}, \qquad (4)$$

where κ_ν is the mass absorption coefficient of the dust, R_{dg} is the dust-to-gas ratio (assuming 10% Helium), and $B_\nu(T_d)$ is the Planck function at the dust temperature, T_d. Using the same values for the above equation as found in Garay et al. (2002), we arrive at a mass estimate

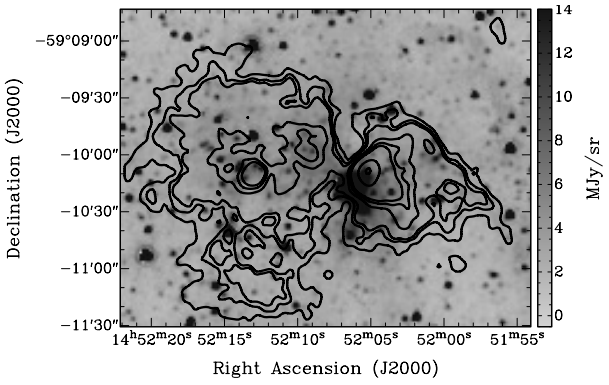

FIG. 11.— A GLIMPSE 4.5 μm image of IRAS 14482-5857, overlaid with same (white) ATCA contours as in Figure 8.

for IRAS 14482–5857, parameterised as a function of the assumed distance of 12.7 kpc (as suggested by the 12CO analysis in Section 3.2.2) of:

$$M_g \sim 1.3 \times 10^4 \left(\frac{D}{12.7 \text{ kpc}}\right)^2 \text{ M}_\odot. \quad (5)$$

It must be explicitly noted, however, that even assuming a distance of 12.7 kpc, the above determination is dependant on $R_{dg}\kappa_\nu$, which is highly uncertain (Garay et al. 2002). Hence we have also obtained mass estimates for IRAS 14482–5857 from the 12CO data.

4.2.2. *12CO and 13CO Optical Depth Analysis and Mass Estimates*

From the fitting of the 12CO and 13CO line presented in Section 3.2.2, we obtain an estimate of the optical depth of the 13CO line from:

$$\tau(\text{13CO}) = \frac{T_A(\text{13CO})}{T_A(\text{12CO})} \sim 0.3, \quad (6)$$

where T_A(13CO) are the fitted brightness-temperatures obtained from fitting the line profiles presented in Figure 6, and assumed to be representative of the cloud as a whole. Assuming a ratio of Carbon 12 to its isotope of $X_{12/13} = 54$ (Burton et al. 2013), we then obtain an optical depth for the main line of $\tau(\text{12CO}) = \tau(\text{13CO})X_{12/13} \sim 14$. This shows that the 12CO line is optically thick, but that the 13CO is optically thin for this cloud. Using the empirical relation describing the CO-to-H_2 conversion factor known as the X-factor from Bolatto et al. (2013) of $X_{\text{12CO}} = 2 \times 10^{20}$ cm^{-2} (K km/s)$^{-1}$, we find a mass for the cloud of $\sim 2 \times 10^4$ M$_\odot$, similar to that derived from the dust flux densities in the previous section. We note that a more detailed analysis, such as that laid out in Burton et al. (2013) (and references therein), or virial mass estimates using the line parameters described in Section 3.2.2, also arrive at a similar mass. This mass also suggests the reason that the HOP survey did not observe NH_3 emission towards this source.

4.3. *Radio and FIR-derived parameters*

TABLE 3
DERIVED PARAMETERS OF THE UCHII REGIONS.

Region – (1)	Size (pc) (2)	EM (pc cm^{-6}) (3)	n_e (cm^{-3}) (4)	N_{Ly} (s^{-1}) (5)	Spectral Type (6)
All	14.5×11	1.4×10^5	96	7×10^{47}	B0.5
A	0.95×0.80	5×10^6	2.3×10^3	3×10^{46}	B0
B	0.48×0.43	3.5×10^7	8.8×10^3	5×10^{48}	O8
C	1.2×0.61	4×10^5	7×10^2	2×10^{47}	B0

Sections 3.2.2 and 3.2.3 strongly suggest that the emission from this region comes from a distance of ~ 12.7 kpc. This implies spatial dimensions for IRAS 14482–5857 $r \sim 11 \times 14.7$ pc for an angular source extent of $3' \times 4'$. Figures 2 and 3 and Table 1 also show that there are three bright peaks of radio emission embedded within IRAS 14482–5857. Here we derive simple parameters for these regions assuming (as the spectral index maps in Figure 4 and integrated flux densities suggest) that these regions are HII regions. We also derive the same parameters for the region as a whole.

From the source spectrum derived in the previous section and shown in Figure 12, we find that IRAS 14482–5857 has an emission measure of $\sim 1.4 \times 10^5$ pc cm^{-6}, an electron number density of ~ 96 cm^{-3}, and an ionising photon production rate of $\sim 7 \times 10^{47}$ s^{-1}. Assuming that the region as a whole is excited by a single zero-age main sequence star, it would be of spectral type B0.5. Table 3 shows the parameters derived for each of the compact sources within IRAS 14482–5857. This shows that IRAS 14482–5857 consists of three UCHII regions (the bright peak sources A, B, and C) embedded within an HII region. It also shows that, if the components that can be classed as UCHII regions are excited by individual zero-age main sequence stars, that the rates of UV photons required to ionise them imply spectral types of said stars of at least B0/1, except for source B, which is strong and compact, and at this assumed distance implies a star of spectral type O8.

4.4. *The Nature of IRAS 14482–5857*

The nature of the IRAS 14482–5857, based on the evidence elucidated above, are strongly suggestive of massive star formation. Walsh et al. (1997) suggest that this source is an UCHII region based on the IRAS colours and the Wood-Churchwell relation. However, several studies of 6.7 GHz methanol maser emission towards this source failed to find any emission down to a limiting flux of 300 mJy/beam (c.f. Section 3.2.4). We suggest that this resulted in this source being overlooked as a site of star formation. Evidence of IRAS 14482–5857 being a site of *massive* star formation is indicated by the following:

1. 12CO and 13CO observations showing strong emission towards the peaks of the radio continuum, which are dominated by emission at a velocity centroid of $V_{LSR} = -1.1$ km/s, with the 13CO line not being able to be fitted for the velocity centroids at $V_{LSR} = -41.6$ and -50.2 km/s at all (though we note that this is probably due to the noise in the 13CO cubes. The derived (hydrogen) column density and mass (viz. $N_{H_2} \sim 1.5 \times 10^{21}$ cm^{-2}

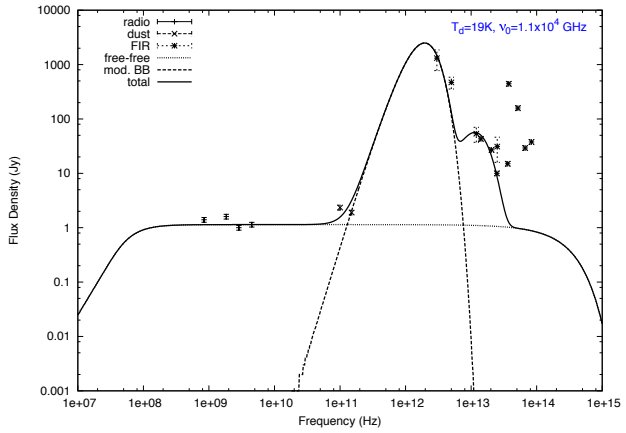

FIG. 12.— Total spectral energy distribution (SED; solid black line) of IRAS 14482–5857 from radio continuum through to the IR. Plus signs mark the radio (843 to 4500 MHz), crosses the dust emission at 100 and 150 GHz from Culverhouse et al. (2011) and stars mark the IRAS, MSX and GLIMPSE fluxes as described in Table 2. The dotted curve is optically thin thermal bremsstrahlung emission modelled by "bootstrapping" the flux to the 4500 MHz PMN datum (see text for more details). The dashed curve is a fit to the spectrum using two modified blackbody functions of the form $B_\nu(T_d)1-\exp[-(\nu/\nu_0)^\beta]$, with different temperatures. The fit parameters for the colder component are shown in the top right-hand corner.

$\sim 2\times10^4$ M$_\odot$) are commensurate with massive star forming regions.

2. The presence of H_2O maser emission towards this source (c.f. Section 3.2.3). The presence of the strong 12CO emission at a velocity centroid of $V_{LSR} = -1.1$ km/s suggests that the velocity of the maser is not significantly displaced from velocity of the star-forming region itself.

3. A dust-derived cloud mass and temperature of $\sim 10^5$ M$_\odot$ and 110 K, respectively.

4. The implied size, emission measure, electron number density and ionising photon production rate derived from the strong, compact radio continuum sources being representative of UCHII regions ionised by O/B stars.

5. The association of the brightest UCHII region with a bright 4.5 μm source, which may be producing outflow-like structures observed at 8 and 24 μm.

We note that the image in Figure 11 is subject to projection effects that may mimic such an outflow-like structure, so that this feature should be investigated further, but is nevertheless interesting. The UCHII regions are surrounded by diffuse radio emission that itself can be considered an HII region. This suggests, along with the bi-lobal radio structure that is seen perpendicular to the strong 8 and 24 μm emission, that this source is a site of massive star formation at an advanced stage of star formation. One possible objection to this hypothesis is that there are no class I methanol masers, which are known to be exclusively associated with high mass star formation (Breen et al. 2013). However, the well known star forming region, Orion Source I, which is forming massive stars, does not contain methanol maser emission (Goddi et al. 2009; Matthews et al. 2010)

5. CONCLUSIONS

IRAS 14482–5857 has been the subject of few searches for southern sites of star formation even though it possessed IRAS colours suggestive of star formation, as the lack of 6.7 GHz methanol maser emission (down to a limiting flux density of 300 mJy/beam) meant that this source was not investigated further. We have presented here new evidence that indeed IRAS 14482–5857 is a site of massive star formation. Our results can be summarised as follows:

1. We have presented new, serendipitous ATCA observations of IRAS 14482–5857 at 1–3 GHz that are an order of magnitude higher in resolution ($\sim 10''$) and sensitivity (~ 100 μJy/beam) than available archival data. These observations reveal that this source possesses a complex, bi-lobal morphology that is, spectrally, dominated by optically thin free-free emission in the broad, low-surface-brightness bubbles, strongly suggestive of an extended, classical HII region. Embedded within this extended envelope are three compact sources that are suggestive of UCHII regions.

2. Spurred by the complex radio morphology, we have performed a detailed literature search and assembled a data-set that includes infrared data from 3.5 to 100 μm, radio continuum to millimetre radio data from 843 MHz to 150 GHz, as well as maser and molecular line data from the HOPS and Mopra Southern Galactic Plane CO Surveys

3. The molecular line data, principally the Mopra Southern Galactic Plane CO Survey data, reveals a complex morphological structure. Towards the brightest radio peak, the spectrum of the 12CO emission exhibits three peaks, two near $V_{LSR} \sim -42$ km/s, and one near $V_{LSR} \sim 0$ km/s. The – albeit noisier – 13CO spectrum, however, exhibits only a single peak structure centred near the $V_{LSR} \sim 0$ km/s component of the 12CO spectrum.

4. Fitting the 12CO and 13CO spectra, we find that the (dimmer) peak at ~ -42 km/s line emission can be fit by a two-component Gaussian, with velocity centroids at $V_{LSR} = -41.6 \pm 0.2$ km/s and $V_{LSR} = -50.2 \pm 0.2$ km/s. These peaks possess a brightness temperature of $T_{mb} = 4.0 \pm 0.1$ K and a full-width at half-maximum (FWHM) of $\sigma_{FWHM} = 1.3 \pm 0.1$ km/s for the former, and $T_{mb} = 3.1 \pm 0.2$ K and $\sigma_{FWHM} = 1.5 \pm 0.1$ km/s for the latter peak. We find a bright peak of 12CO data located at $V_{LSR} = -1.1 \pm 0.1$ km/s that is well fit using a brightness temperature of $T_{mb} = 5.2 \pm 0.2$ K, and a FWHM width of $\sigma_{FWHM} = 1.5 \pm 0.1$ km/s. The 12CO isotopologue 13CO, also reveals line emission that is well-fit to $T_{mb} \sim 1.4 \pm 0.1$ K at a velocity centroid of $V_{LSR} = -0.9 \pm 0.1$ km/s and a FWHM width of $\sigma_{FWHM} = 1.0 \pm 0.1$ km/s, suggesting that the bulk of the mass is indeed at the

farther distance. We then used a water maser catalogued with the HOP survey that is positionally coincident with IRAS 14482–5857, with a peak flux density of 5.1 Jy at –3.3 km/s with a line-width of 1.0 km/s. We thus take the cloud to be at a velocity of $V_{LSR} = -1.1$ km/s, which places it at a distance of ~ 12.7 kpc.

5. Using the 12CO and 13CO data, we have used two methods for estimating the hydrogen column density and mass towards IRAS 14482–5857, which we find give average values of $N_{H_2} \sim 1 \times 10^{21}$ cm^{-2} and $\sim 2 \times 10^4$ M$_\odot$.

6. Using the distance estimate obtained from the 12CO data, we thus fit sizes for the strong radio continuum sources of $\lesssim 1$ pc, strongly suggestive of UCHII regions. We then derive parameters for these sources: emission measures of $\sim 10^6$ pc cm^{-6}, electron number densities ($\sim 10^3$ cm^{-3}), and rates of ionising photon production of $\sim 10^{46-48}$ s^{-1}, consistent with OB stars.

7. 3-colour images of the region at 4.5, 8 and 24 μm reveal a complex far-infrared (FIR) spectromorphology. The 4.5 μm emission reveals a strong, compact source located at a minimum of the radio contours, indicative of a young stellar object. Emanating from the point-source is what appears to be a outflow-like structure, which seems to align with the brightest of the three radio continuum peaks found in the object. The point source and outflow-like structure appears to be surrounded by a region of hot dust, as indicated by the abundance of 24 μm emission found there. The emission within the diffuse 1–3 GHz radio contours is dominated by 24 μm emission, suggesting that the radio bubbles are "filled" with hot dust. Intersecting perpendicularly the lobular regions of hot dust is a region dominated by PAH emission, which also envelopes the diffuse radio emission with many wispy segments.

8. Spectrally, the region as a whole is well fit by an optically thin thermal bremsstrahlung and two-component modified blackbody spectrum. The thermal bremsstrahlung component implies an emission measure of $\sim 1.4 \times 10^5$ pc cm^{-6}, an electron density of ~ 96 cm^{-3}, a dust mass of $\sim 6.701 \times 10^5$ M$_\odot$, and a production rate of ionising photons of N_{Ly} of $\sim 7 \times 10^{47}$ s^{-1} for this source over its entire $3' \times 4'$ extent. The dust/FIR part of the spectrum is well fit by a two-component greybody with temperatures of $T_d = 19$ and 110 K, respectively, strongly suggestive of massive star formation.

In totality, the evidence – distance estimates, strong radio sources that are consistent with UCHII regions, the presence of a water maser, a high mass derived from the 12CO observations, and a high dust temperature – strongly indicate that IRAS 14482–5857 is a site of massive star formation.

ACKNOWLEDGMENTS

We would like to thank the anonymous referee whose comments made the paper immeasurably better. DIJ would like to thank Petter Hofverberg for assistance with the observations and Ciriaco Goddi and Jürgen Ott for enlightening discussions and a critical reading of the manuscript. This research has made use of the SIMBAD database, operated at CDS, Strasbourg, France. The Australia Telescope is funded by the Commonwealth of Australia for operation as a National Facility managed by CSIRO.

REFERENCES

Bocchino, F., Parmar, A. N., Mereghetti, S., et al. 2001, A&A, 367, 629
Bock, D. C.-J., Large, M. I., & Sadler, E. M. 1999, AJ, 117, 1578
Bolatto, A. D., Wolfire, M., & Leroy, A. K. 2013, ARA&A, 51, 207
Breen, S. L., Caswell, J. L., Ellingsen, S. P., & Phillips, C. J. 2010a, MNRAS, 406, 1487
Breen, S. L., Ellingsen, S. P., Caswell, J. L., & Lewis, B. E. 2010b, MNRAS, 401, 2219
Breen, S. L., Ellingsen, S. P., Contreras, Y., et al. 2013, MNRAS, 435, 524
Burton, M. G., Braiding, C., Glueck, C., et al. 2013, Pub. Astron. Soc. of Aust., 30, 44
Caswell, J. L. 1998, MNRAS, 297, 215
Churchwell, E., Babler, B. L., Meade, M. R., et al. 2009, Pub. of the Astronom. Soc. of the Pac., 121, 213
Crocker, R. M., Jones, D. I., Melia, F., Ott, J., & Protheroe, R. J. 2010, Nature, 463, 65
Culverhouse, T., Ade, P., Bock, J., et al. 2010, ApJ, 722, 1057
—. 2011, ApJS, 195, 8
Cyganowski, C. J., Whitney, B. A., Holden, E., et al. 2008, AJ, 136, 2391
Garay, G., Brooks, K. J., Mardones, D., Norris, R. P., & Burton, M. G. 2002, ApJ, 579, 678
Goddi, C., Greenhill, L. J., Chandler, C. J., et al. 2009, ApJ, 698, 1165
Green, J. A., Caswell, J. L., Fuller, G. A., et al. 2012, MNRAS, 420, 3108
Hill, T., Burton, M. G., Minier, V., et al. 2005, MNRAS, 363, 405
Hindson, L., Thompson, M. A., Urquhart, J. S., et al. 2012, MNRAS, 421, 3418
Jones, P. A., Burton, M. G., Cunningham, M. R., et al. 2012, MNRAS, 419, 2961
Matthews, L. D., Greenhill, L. J., Goddi, C., et al. 2010, ApJ, 708, 80
Mauch, T., Murphy, T., Buttery, H. J., et al. 2003, MNRAS, 342, 1117
Maxted, N. I., Rowell, G. P., Dawson, B. R., et al. 2012, MNRAS, 422, 2230
Menten, K. M. 1991, ApJ, 380, L75
Molinari, S., Brand, J., Cesaroni, R., & Palla, F. 1996, A&A, 308, 573
Nicholas, B., Rowell, G., Burton, M. G., et al. 2011, MNRAS, 411, 1367
Ossenkopf, V., & Henning, T. 1994, A&A, 291, 943
Pineda, J. E., Caselli, P., & Goodman, A. A. 2008, ApJ, 679, 481
Tielens, A. G. G. M. 2008, Ann. Rev. Astron. & Astro., 46, 289
Voronkov, M. A., Caswell, J. L., Ellingsen, S. P., Green, J. A., & Breen, S. L. 2014, ArXiv e-prints, arXiv:1401.5179
Walsh, A. J., Hyland, A. R., Robinson, G., & Burton, M. G. 1997, MNRAS, 291, 261
Walsh, A. J., Breen, S. L., Britton, T., et al. 2011, MNRAS, 416, 1764
Wood, D. O. S., & Churchwell, E. 1989, ApJS, 69, 831
Wright, A. E., Griffith, M. R., Burke, B. F., & Ekers, R. D. 1994, ApJS, 91, 111
Zinnecker, H., & Yorke, H. W. 2007, AR&AA, 45, 481